Development and Assessment of a Single-image Fringe Projection Method for Dynamic Applications

by M. A. Sutton, W. Zhao, S. R. McNeill, H. W. Schreier and Y. J. Chao

ABSTRACT—A single-image fringe projection profiling method suitable for dynamic applications was developed by combining an accurate camera calibration procedure and improved phase extraction procedures. The improved phase extraction process used a modified Hilbert transform with Laplacian pyramid algorithms to improve measurement accuracy. The camera calibration method used an accurate pinhole camera model and pixel-by-pixel calibration of the phase-height relationship. Numerical simulations and controlled baseline experiments were performed to quantify key error sources in the measurement process and verify the accuracy of the approach. Results from numerical simulations indicate that the resulting phase error can be reduced to less than 0.02 radians provided that parameters such as fringe spacing, random measured intensity noise, fringe contrast and frequency of spatial intensity noise are carefully controlled. Experimental results show that the effects of random temporal and spatial noise in typical CCD cameras for single fringe images limits the accuracy of the method to 0.04 radians in most applications. Quantitative results from application of the fringe projection method are in very good agreement with numerical predictions, demonstrating that it is possible to design both a fringe projection system and a measurement process to achieve a prespecified accuracy and resolution in the point-to-point measurement of the spatial (X, Y, Z) positions.

KEY WORDS—Profile measurement, single-image fringe projection, camera calibration, fringe extraction, Hilbert transform, Laplacian pyramid

Introduction

Noncontacting measurement of three-dimensional shape or object profile is important in many areas, including medicine, on-line inspection, computer-aided design/manufacturing and reverse engineering. With recent advances in computing technology, some of these techniques have become automated, easier to use in applications and more efficient in data reduction, which has resulted in the development of full-field optical techniques that are being used for real-time profile measurements in a wide range of settings, including industry, government and university laboratories.

M. A. Sutton (SEM Member) is a Faculty Member, Department of Mechanical Engineering, University of South Carolina, Columbia, SC 29208. W. Zhao is an Engineer, SolidWorks Corporation, Concord, MA 01742. S. R. McNeill (SEM Member) is a Faculty Member, H. W. Schreier (SEM Member) is a Graduate Student and Y. J. Chao (SEM Member) is a Faculty Member, Department of Mechanical Engineering, University of South Carolina, Columbia, SC 29208.

The form of the projected light pattern (e.g., random pattern, fringes) is one way to differentiate between various noncontacting, three-dimensional profilometers. Using this approach, one category can be described as nonfringe methods. Included in this group are methods such as three-dimensional digital image correlation using either one camera[1] or two cameras[2–4] whereby a random speckle pattern is used to determine the object profile. In general, methods of this type are relatively robust and capable of achieving high accuracy for many applications. However, data reduction requires intensive computational effort, and the finite size of subregions used in the method makes it more difficult to locate and traverse edges.

The other category, fringe methods, includes methods such as shadow moiré[5–7] and grating projection.[8] These methods extract height distribution information from fringe patterns through processing of the deformed fringe patterns to identify local variations in height. One advantage of these methods is that few calculations are required to convert image data into profile information. In fact, the methods have been used for real-time inspection in many applications.

One popular method for extracting phase information from fringe patterns is known as phase shifting.[9–14] This method requires several (at least three) images with known or unknown phase shifts between subsequent images. For profiling purposes, the fringe pattern is usually translated by mechanical shifting of the grating plate. In these cases, the accuracy of the extracted phase is limited by the accuracy of the translational process. Recent studies[15–17] have shown that high-resolution programmable projectors can be used to electronically shift a projected grid with reasonable accuracy.

Fourier transforms are also used to extract phase information. This technique was proposed by Takeda, Ika and Kobayasha[18] in 1982 and has the advantage of using only one fringe pattern image to extract the phase distribution. The image is processed in the frequency domain using fast Fourier transforms (FFTs). Mathematically, this method is closely related to the Hilbert transform used in this work.[19,20]

More recently, Tang and Hung[21] proposed a low-pass filter method, which is performed in the spatial domain on one fringe pattern. The method is similar to the FFT approach. Thus, selection of an appropriate filtering window is also a critical problem in practice when using this method. Toyooka and Iwasa[22] proposed spatial phase detection in 1986. This technique acquires phase at the midpoint of fringe intervals. All points in between the midpoint locations are interpolated assuming a linear phase change between fringes. Although relatively fast, the interpolation procedure limits the accuracy of the extracted phase.

Recently, a one-step phase shift projection procedure was proposed by Gu *et al.*[23] Unfortunately, a requirement of this method is that the pitch of the fringe pattern be either four pixels or eight pixels, severely limiting the method for many applications.

As noted above, much work has been done to develop robust, fast algorithms for fringe analysis. However, much less work has been done to improve the phase-height relationship representation for the experimental setup so that highly accurate spatial position data can be acquired for object reconstruction using a single image, such as is needed for dynamic applications.

In the enclosed work, an accurate camera calibration procedure and improved phase extraction procedures using a modified Hilbert transform with Laplacian pyramid algorithms[24] were developed and successfully demonstrated for measurement of the full (X, Y, Z) positions of surface points using single-image fringe projection profiling methods suitable for dynamic applications. Detailed numerical simulations and controlled baseline experiments were performed to quantify the key error sources in the measurement process and verify the accuracy of the approach.

Fringe Projection System

The fringe projection system developed for this work was designed for profiling of static objects and for measurements of dynamic shape changes. The system uses only single fringe images, as opposed to multiple, phase-shifted fringe patterns. Thus, the focus of this research was to obtain optimal accuracy from single fringe images.

A laboratory-scale fringe projection system is shown in Fig. 1. The system consists of a CCD camera with a regular photographic lens (Nikon 200 mm) and a projector assembled from standard optical components. Also shown in Fig. 1 is a calibration plane mounted to a translation stage.

Basic Equations and System Calibration

In this work, a pinhole camera model[2] was used for the camera system because it has been shown to be an accurate method for mapping positions in three-dimensional space
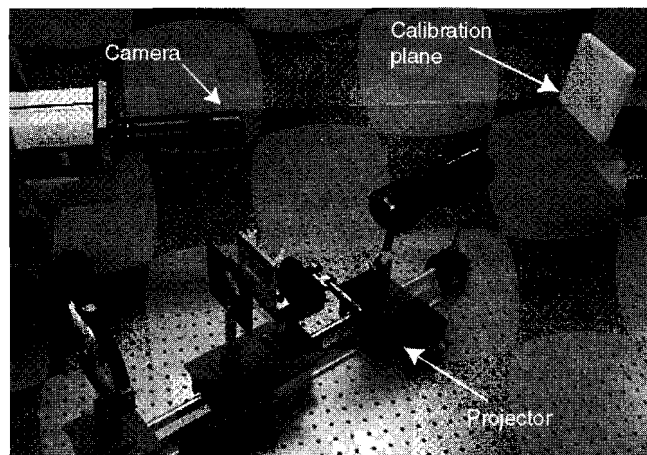

Fig. 1—Photograph of laboratory setup

into camera coordinates. The pinhole camera is described by its optical center, o_x, o_y, the aspect ratio of the sensor, μ, the focal length, f, and a lens distortion coefficient, κ. To calculate the pixel coordinates (x, y) of a point $\mathbf{X} = (X, Y, Z)$ in global coordinates, a rotation matrix $[\mathbf{R}]$ and a translation vector $\mathbf{T}$, which relate the global coordinate system and the sensor coordinate system, are introduced. Then, neglecting the distortion, the image of a point $\mathbf{X}$ is given by

$$
x = \frac{f}{(\mathbf{r}_3^T \bullet \mathbf{X} - t_3)}(\mathbf{r}_1^T \bullet \mathbf{X} - t_1)o_x
$$
$$
y = \frac{f}{\mu(\mathbf{r}_3^T \bullet \mathbf{X} - t_3)}(\mathbf{r}_2^T \bullet \mathbf{X} - t_2)o_y,
$$
(1)

where $\mathbf{r}_i$ denote the rows of the rotation matrix and (t_1, t_2, t_3) are components of $\mathbf{T}$. If the Z-coordinate of a point in the global coordinate system and its image (x, y) are known, the global X and Y coordinates of the point can be calculated from eq (1) as follows:

$$
X = \frac{Z - \mathbf{r}_3^T \bullet T}{\mathbf{r}_3^T \bullet (x - o_x, \frac{y - o_y}{\mu}, f)^T} \bullet
$$
$$
\left\{ \mathbf{r}_1^T \bullet (x - o_x, \frac{y - o_y}{\mu}, f)^T \right\} + \mathbf{r}_1^T \bullet \mathbf{T}
$$
$$
Y = \frac{Z - \mathbf{r}_3^T \bullet T}{\mathbf{r}_3^T \bullet (x - o_x, \frac{y - o_y}{\mu}, f)^T} \bullet
$$
$$
\left\{ \mathbf{r}_2^T \bullet (x - o_x, \frac{y - o_y}{\mu}, f)^T \right\} + \mathbf{r}_2^T \bullet \mathbf{T},
$$
(2)

where $\mathbf{r}_i^T$ denote the transpose of the rows of the rotation matrix and $\bullet$ denotes the inner product of the two vectors. Equation (2) suggests the following procedure for calibrating the fringe projection system:

1. Calibrate the intrinsic camera parameters $(o_x, o_y, f, \mu, \kappa)$ through calibration techniques as described in Refs. 2, 3 and 4.

2. Calibrate the extrinsic parameters of the system ($[\mathbf{R}]$, $\mathbf{T}$) with respect to a reference plane. The extrinsic parameters can also be obtained by the calibration procedures.[2,3]

3. For every pixel in the image, obtain a functional form $Z = f(\varphi)$, where φ is the phase of the fringe image. This is accomplished by translating the reference plane along its normal and recording fringe images at known distances Z_i throughout the depth range of interest. After phase extraction and unwrapping, the function $Z = f(\varphi)$ can be obtained by fitting a low-order polynomial.

After calibration, the phase extracted from a measurement fringe image can be used to calculate the Z position for a given pixel (x, y) using the calibration polynomial. Then, eq (2) can be used to calculate the X and Y position of the corresponding measurement point.

Importance of Z Correction to (X, Y) Positional Data

As shown in eq (2), the (X, Y) coordinates of an object point are a strong function of the Z position if the range of Z positions is not negligible compared to the distance between object and camera. Thus, apparent (x, y) positions must be corrected using the measured Z height to obtain accurate (X, Y, Z) measurements. Furthermore, Fig. 2 clearly shows that all measured (X, Y, Z) coordinates for every point on the object are related to the measurement system parameters. Hence, any simple estimation of the system parameters or assumption with regard to the geometry of the experimental setup will introduce errors in the final measured data. Thus, calibration of both the camera system and the phase-height relationship is critical to the accurate profiling of a component.

Figure 2 illustrates the differences between the measured X-coordinates, with and without the Z-coordinate correction. Point A on the object surface is imaged as point B on the image plane of the camera. Point B is off the optical axis of the camera by a distance x in the x-direction. Traditionally, the X position for A is calculated by multiplying the magnification factor f_M by x, that is, $X_{no-cr} = f_M \bullet x$, where f_M is calibrated on the reference plane and $f_M = L/d$. To properly account for the depth effects, the X-coordinate of point A should be calculated by $X_{cr} = (L - Z)/d \bullet x$, where the difference between X_{no-cr} and X_{cr} is

$$\Delta X_{error} = X_{cr} - X_{no-cr} = \frac{Z}{d}x. \qquad (3)$$

For a typical test, in which $d = 20,000$ pixels, $Z = 10$ mm and $x = 250$ pixels, the positional error in X or Y can be as large as 125 μm, which cannot be ignored when making precision measurements of an object's shape.

Phase Extraction

As noted earlier, multiple phase-shifted fringe images cannot be used for shape measurement in dynamic applications.
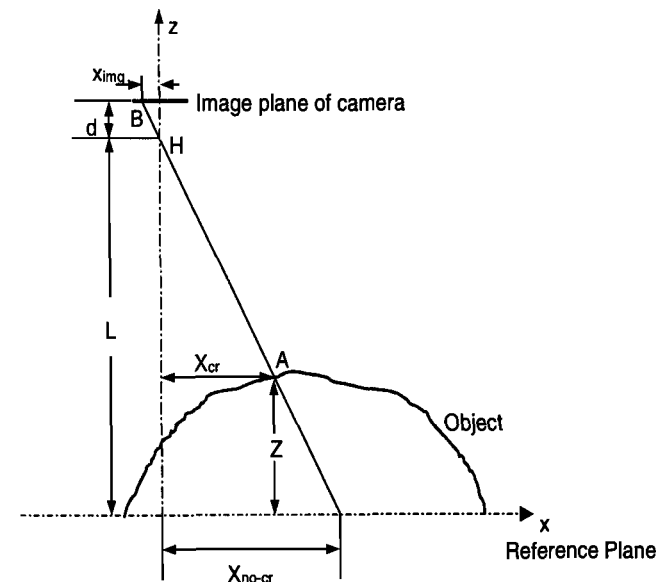

Fig. 2—Correction for X-coordinate

Thus, in this work, emphasis is placed on accurate shape measurement and phase extraction using single fringe images.

For such applications, there are two steps in the phase extraction process. First, phase information is extracted from a projected fringe pattern that is "wrapped" from $-\pi$ to $+\pi$ due to well-known characteristics of inverse trigonometric functions. Second, the original phase is "unwrapped" to obtain a continuous phase map as a function of height. Simple unwrapping techniques unwrap the phase on a line-by-line basis. However, new approaches have been developed recently to deal with fringe discontinuities and to more accurately extract phase over a wider range of object height variations.[25–31] Unfortunately, many of the more elaborate phase-unwrapping techniques are not applicable for single-image applications.[30]

In this work, a Hilbert transformation approach is proposed for obtaining phase information from a projected fringe pattern and a flood-fill algorithm is implemented for phase unwrapping.

Numerical Phase Shifting

Various methods for phase extraction from a single fringe image exist, most notably the Fourier transform method introduced by Takeda, Ika and Kobayasha.[18] A method mathematically closely related to the Fourier transform method can be implemented in the spatial domain using Hilbert filters.[22] The ideal Hilbert filter introduces a phase shift of $\pi/2$ without altering the signal amplitude and removes the DC component of the signal. For a fringe image

$$I(x) = a(x) + b(x)\cos(\phi(x)), \qquad (4)$$

the background term $a(x)$ can be removed by an appropriate high-pass filter provided that the background intensity varies slowly compared to the frequency of the fringes. After application of the high-pass filter to eq (4), one obtains a fringe image

$$I_1(x) = b_1(x)\cos(\phi(x)), \qquad (5)$$

which can then be passed through the Hilbert filter to obtain

$$I_2(x) = -b_2(x)\sin(\phi(x)). \qquad (6)$$

The principal value of the phase is given by

$$\phi(x) = \operatorname{atan}\frac{-I_2(x)}{I_1(x)}. \qquad (7)$$

Inspection of eqs (4) through (7) demonstrates that the accuracy of phase values obtained in this manner is highly dependent on (1) preservation of the signal amplitude, $b_1(x)$, during the shift process, (2) accuracy of the numerical phase shift and (3) elimination of the background intensity. In the following sections, the Hilbert transform (filter) is described and its effectiveness is discussed in detail.

Hilbert Transform

The transfer function for an ideal Hilbert filter is shown in Fig. 3. Here, the wave number is the normalized ratio k_s/k_N, where k_s and k_N are the signal and Nyquist wave numbers, respectively (e.g., for a CCD camera, k_N is $\pi/2$ pixels^{-1}).
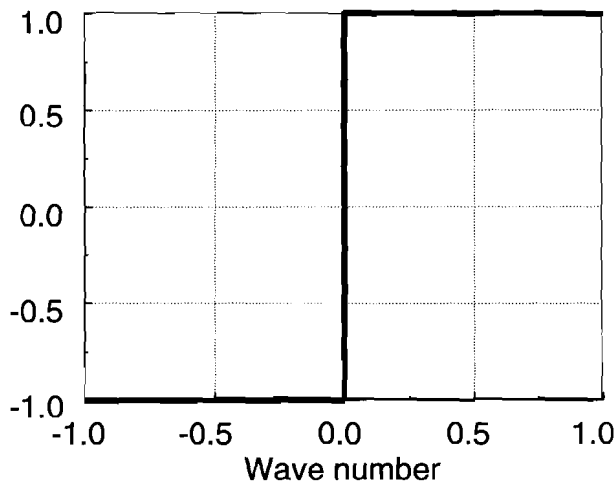
Fig. 3—Imaginary part of the ideal transfer function for the Hilbert filter (the real part is zero)

Because convolution of a signal with a convolution mask in the spatial domain corresponds to multiplication of the Fourier transforms in the frequency domain, we can write

$$\int g(x)H(x - y)dx = F(g(x)) * F(H(x)), \qquad (8)$$

where $F()$ is the Fourier transform operator, $H(x)$ is the convolution mask or point spread function and $F(H(x))$ is the transfer function. Because the real part of an ideal Hilbert filter is zero and its magnitude is identical to one, multiplication of a signal by the Fourier transform of this transfer function results in a phase shift of $\pi/2$ while preserving the signal amplitude.

Because the point spread function $H(x)$ decreases only slowly with $1/x$, the ideal Hilbert filter cannot be accurately implemented with a compact convolution kernel. However, it is possible to construct compact Hilbert filter kernels with minimal amplitude error in a certain wave number range. For symmetry reasons, a filter kernel of double step-width and odd symmetry is chosen. As an example, a four-coefficient filter can be expressed by

$$\begin{bmatrix} -h_4 & 0 & -h_3 & 0 & -h_2 & 0 & -h_1 & 0 \\ & & & & & & & \\ h_1 & 0 & h_2 & 0 & h_3 & 0 & h_4 \end{bmatrix}, \qquad (9)$$

where the dot indicates the center pixel. The corresponding transfer function can be written as

$$\hat{H}(\tilde{k}) = \sum_{r=1}^{4} h_r \sin\left((2r - 1)\pi\tilde{k}\right). \qquad (10)$$

Appropriate coefficients h_r are found through a weighted least squares optimization, where the weighting function is used to control the wave number range for which the filter is to be optimized. For details of the optimization procedure, as well as further optimization through recursive pre-filters, we refer to Jaehne.[20] As an example, an optimized transfer function for the coefficients $h_1 = 0.62078$, $h_2 = 0.168256$, $h_3 = 0.0629796$ and $h_4 = 0.0190886$ is shown in Fig. 4. Because the optimized filter is not unity for all wave numbers,

the signal amplitude will be slightly altered. For example, for the wave number range of [0.2, 0.8] corresponding to wavelengths between 3 and 10 pixels, the amplitude errors are below 1 percent.

With regard to the selection of a spatial domain filter, in place of a frequency domain filter, it is noted that the remarkable accuracy obtained with the Hilbert transform is achieved with only four multiplications and four additions per pixel, allowing for extremely fast and accurate fringe pattern analysis.

DIRECT IMPLEMENTATION

If the frequencies of the fringes are contained within the optimal work range of the Hilbert filter, the Hilbert filter can be directly applied to the fringe image. As can be seen from the transfer function of the Hilbert filter (Fig. 4), the filter can also be used to remove low-frequency background components. Thus, a first application of the filter to the fringe image given by eq (4) will yield

$$I_1(x) = -b_1(x) \sin(\phi(x)) \qquad (11)$$

and a subsequent application of the filter

$$I_2(x) = -b_2(x) \cos(\phi(x)). \qquad (12)$$

The principal value of the phase for this case is given by

$$\phi(x) = \operatorname{atan} \frac{I_1(x)}{I_2(x)}. \qquad (13)$$

The limitations of this approach are the relatively narrow range of fringe spacing that can be accurately processed and the requirement of virtually constant background intensity, since the transfer function of the Hilbert filter increases rapidly at low wave numbers (see Fig. 4).

PYRAMID IMPLEMENTATION

To overcome the restrictions of the direct approach, the fringe image can first be decomposed into a Laplacian pyramid.[24] The Laplacian pyramid provides an efficient band-pass decomposition of the fringe image combined with appropriate subsampling of lower frequency components. The name pyramid refers to the pyramid that would be formed if the increasingly smaller image layers were stacked upon each other. To obtain the Laplacian pyramid, the Gaussian pyramid[24] is constructed first. By applying a low-pass filter to the original image and then subsampling the image by a factor of two, the first layer of the Gaussian pyramid is calculated. This procedure is recursively repeated with the newly constructed layers until no further subsampling is possible. The low-pass filtering ensures that no aliasing occurs due to subsampling.

Each layer of the Laplacian pyramid is constructed as the difference image between each layer of the Gaussian pyramid and its next higher layer. To perform the subtraction, the next higher layer is first scaled by a factor of 2, using appropriate interpolation filters. The highest layer of the Laplacian pyramid is identical to the highest layer of the Gaussian pyramid. A pyramid-merging process can be used to obtain the original image. The merging process is performed by adding all layers of the Laplacian pyramid after proper scaling. The first four layers of a Gaussian and Laplacian pyramid of a
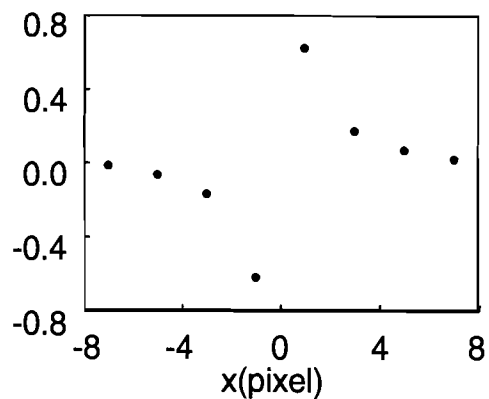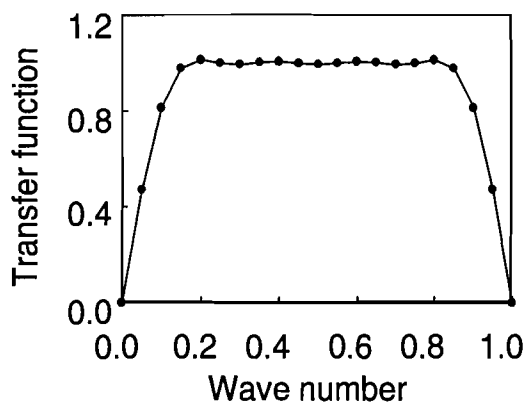
Fig. 4—Transfer function and point spread function for optimized four-coefficient Hilbert filter

Fig. 5—Construction of Gaussian pyramids (top) and Laplacian pyramids (bottom) after images are normalized to the intensity range [0, 255] and higher layers are scaled to the original size

Fig. 6—Maximum phase extraction error as a function of fringe spacing for the direct phase extraction algorithm and the Laplacian pyramid algorithm

fringe image are shown in Fig. 5. One can see that only the first three layers contain fringe information and the fourth layer (and all higher layers) contains lower frequency background information. This observation can be used to remove the background term $a(x)$ from the fringe image by merging only the first three layers of the Laplacian pyramid:

$$I_1(x) = b_1(x)\cos(\phi(x)). \tag{14}$$

The numerically phase shifted image is obtained by individually applying the Hilbert filter to each of the first three layers of the Laplacian pyramid and subsequent merging of the shifted layers. Because the lower frequency fringes are contained in the higher layers of the pyramid and thus subsampled, they lie within the optimal working range of the Hilbert filter on the smaller grid. For instance, a fringe period of 30 pixels in the original image would be found in the third layer of the pyramid with a period of 7.5 pixels, which can be accurately processed by the optimized Hilbert filter.

Accuracy Assessment for Phase Extraction Process Using the Hilbert Filter

There are several sources of error in the process of extracting phase from a projected fringe pattern. In this work, the error sources considered are frequency content of projected pattern, variations in background intensity, variations in amplitude of signal, variations in fringe spacing, digitization and contrast, and random intensity fluctuations. In the following
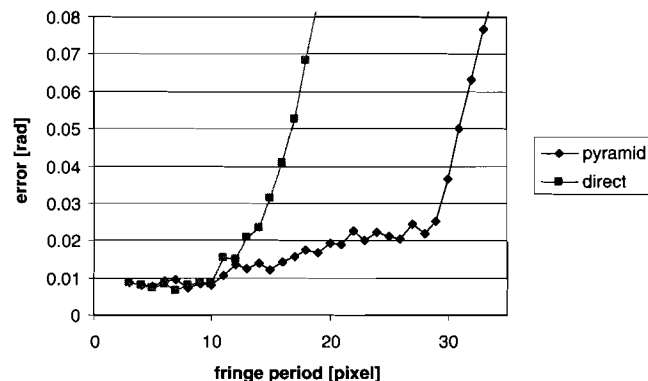
sections, each error source is described and the magnitude of the phase error quantified through numerical simulations.

FRINGE FREQUENCY RANGE FOR ACCURATE PHASE EXTRACTION

Large height variations on a component will result in a substantial change in fringe spacing within the recorded image. To obtain accurate measurements over a large range of height variations, the fringe-processing algorithm must be capable of accurate phase extraction over a wide range of fringe spacing.

Figure 6 shows a comparison of the phase extraction error when analyzing perfect sinusoidal signals having a range of wave numbers for both the direct implementation and the pyramid implementation. In these simulations, the computer-generated, 8-bit test images had constant fringe spacing and amplitude of 64 gray levels with a constant background intensity of 128 gray levels.

As shown in Fig. 6, frequency-dependent errors exist in the phase extraction process due to band-pass characteristics of the Hilbert filter. For both the direct and the pyramid implementation, fringe patterns having wavelengths from 3 to 9 pixels, the phase error is nearly constant at 0.01 radians or $\pi/315$. For wavelengths greater than 10 pixels, Fig. 6 clearly shows that the pyramid algorithm extends the range of acceptable fringe periods (low phase extraction error) from 10 pixels to about 30 pixels, with only a slight increase in error at the lower period lengths.

Finally, it is noted that the Hilbert filter (see Fig. 4) does not fully eliminate components in the range [0.8, 1.0]. Thus, intensity noise having a wavelength between 1 and 1.6 pixels should be minimized to reduce the potential for increased error in the phase extraction process.

EFFECTS OF DIGITIZATION ON SIGNAL CONTRAST AND PHASE ACCURACY

A fringe pattern image, generated with the phase and intensity distribution described in eq (4) and having a wave number $k = 0.20$ ($\lambda = 10$ pixels), is used in these analyses. To isolate the effects of digitization, both $a(x)$ and $b(x)$ are fixed. The form for $I(x)$ is written as

$$\phi(x) = 9.9 \cdot 10^{-9} \cdot x^4 - 9.04 \cdot 10^{-6} \cdot x^3$$
$$+ 2.45 \cdot 10^{-3} \cdot x^2 + 2 \cdot \pi \cdot 0.1 \cdot x \qquad (15)$$
$$I(x) = a + b \cdot \cos(\phi(x)).$$

The phase, $\phi(x)$, is extracted from the fringe pattern image using the procedure described above, unwrapped, and compared with the actual phase given in eq (15). The difference in phase is taken as the error of phase extraction.

To simulate the effects of digitization, floating point format images are generated and then chopped using the INT() function in C language to obtain only integer intensity values corresponding to digitization levels of 2^n, where n is the number of bits used to record an intensity value. For example, an 8-bit sensor would record intensity values in the range 0 to 255. In this analysis, the amplitude of the intensity pattern is maximized and is given by the equation $a = b = 1/2(2^n - 1)$.

Figure 7 shows how accuracy is affected by quantization during the imaging process. As shown in Fig. 7, an increase in the number of sampling bits from 4 (16 gray levels) to 9 (512 gray levels) results in a decrease of the maximum phase error from 0.09 radians to 0.01 radians, with negligible additional error reduction when using up to 14 bits (16,384 gray levels).

EFFECT OF RANDOM NOISE ON PHASE ACCURACY

As shown in Fig. 8, random fluctuations are commonplace in digital cameras. Conceptually, the two sources of random noise are time-varying fluctuations in the sensor values and spatially varying fluctuations due to object surface variability.

Baseline tests indicate that the time variations are random and Gaussian in distribution, with a standard deviation of 0.9 gray levels for an 8-bit Pulnix 9701 CCD camera. Using time averaging to eliminate temporal noise, baseline tests demonstrated that the spatial noise varies randomly, with a standard deviation of approximately 2.2 gray levels for 8-bit recording of a projected fringe pattern on a white, painted planar surface. This level of intensity variation corresponds to a noise-to-signal ratio of 3.6 percent.

To simulate the effects of either spatial or temporal variations in the measured intensity data, Gaussian noise with a zero mean value and a range of standard deviation values was added to the signal generated by eq (4) and the phase extraction process described previously was performed. Fig. 8 shows the relationship between both standard deviation in phase and maximum error in phase and the ratio between the standard deviation of the random noise and the signal's amplitude. Figure 8 was obtained by using 8-bit generated fringe patterns represented in eq (4). Maximum contrast was assumed, and all processing was done using the Hilbert filter with Laplacian pyramid modification.

As shown in Fig. 8, for a fixed digitization level, enhancing fringe contrast without increasing the level of noise will increase the accuracy of the phase extraction process. Similarly, increasing the digitization level without increasing the level of noise will also decrease the noise-to-signal ratio and increase the accuracy of the phase extraction process. As expected, simulations performed with fringe patterns generated with 12 or more bits gave nearly identical results.

Finally, a comparison of the magnitude of the errors introduced by digitization, fringe frequency and random noise clearly shows that random spatial intensity fluctuations are potentially one of the largest sources of phase error.

Experimental Verification

As outlined in the previous section, detailed numerical simulations have been performed to identify error sources and quantify their effects on overall accuracy of the method. In this section, results obtained from camera calibration and
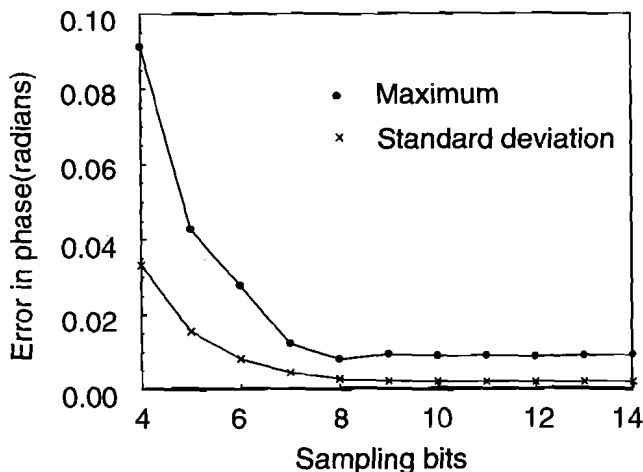
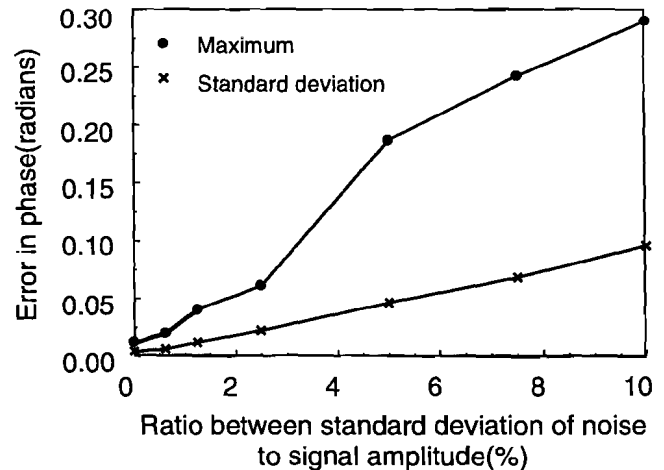Fig. 7—Phase extraction error versus number of sampling bits

Fig. 8—Relationship between phase error and random spatial noise level for $k = 0.2$

a series of baseline experiments are presented, along with comparisons to the error estimates obtained through numerical simulation of the measurement process.

Measurement System Calibration

One approach for calibration of the single-image projection system would be to calibrate both the camera and the projector. If a pinhole model is assumed and the aspect ratio of the camera is determined independently, calibration requires that 20 parameters describing the camera and projector be determined through a nonlinear optimization process. To eliminate the requirement for projector calibration, a two-step calibration process for the fringe projection system was used. First, calibration of the camera parameters was performed. Second, a separate calibration of the phase-height relationship at every pixel location was performed.

CAMERA CALIBRATION

Figure 9 shows a schematic of the setup used for camera calibration. Camera calibration follows the procedures outlined by Helm, Sutton and McNeill,[2] Tsai[3] and Weng, Cohen and Herniou[4] for three-dimensional machine vision. First, as shown in Fig. 9(a), the camera is placed in position and focused on a precision calibration grid such as is shown in Fig. 9(c). The grid is placed approximately where the specimen will be located. Lines on the calibration grid are used to establish the position and orientation of the system coordinate system, with the initial plane of the grid defined as $Z = 0$. A lens with a large f-number is used to increase the depth of field.

To calibrate the camera, a series of images of the calibration grid is acquired at several different relative positions of the grid and camera using the procedure outlined by Helm, Sutton and McNeill.[2] In this regard, it is noted that the ratio of pixel dimensions is determined prior to performing the calibration process. By determining the ratio of pixel dimensions prior to performing the calibration process, a total of nine camera parameters are obtained using the nonlinear optimization process described in Ref. 2.

PIXEL-BY-PIXEL CALIBRATION OF PHASE-HEIGHT RELATIONSHIP

The procedure for pixel-by-pixel calibration of the phase-height relationship is as follows. First, the positions of the camera and projector are fixed and a fringe pattern is projected onto a diffusely reflecting reference plane, as shown in Fig. 9(b). To complete the calibration process, the simplest approach is to ensure that the reference plane remains parallel to the plane of the calibration grid and to know the relative position of the two planes. This is easily achieved by mounting the calibration grid to the reference plane and, after camera calibration, moving the reference plane to compensate for the grid's thickness. Images of the fringe pattern are acquired as the reference plane is translated N times along the direction of the surface normal by known distances, Z_i. Using the phase extraction procedure described previously, the phase-height relationship for each pixel is established by fitting a third-order polynomial to the N pairs of $(Z_i, \Delta\phi_i)$. By storing the polynomial coefficients in a look-up table format, this procedure provides an efficient, accurate method for determining the object distance from the reference plane at each pixel location as a function of phase.

Baseline Experiments

In the following section, results from a series of laboratory experiments are described. The experiments were performed to determine how well the numerical simulations represent the physical situation. In particular, the effects of random noise and contrast were evaluated experimentally.

To minimize the errors associated with higher frequency components, a high-quality sinusoidal grating (HQSG) pattern produced by Sine Patterns LLC is used in this work. Scan data offered by the manufacturer shows that the amplitude ratios among the first-order (a_1/a_1), second-order (a_2/a_1) and third-order (a_3/a_1) harmonics amplitudes are 1, 0.0008 and 0.0004, respectively. Our numerical simulations with these parameters have shown that these higher order harmonics with low amplitude introduce phase extraction errors of less than 0.001 radians.

Random Noise

As shown in Fig. 8, random intensity fluctuations are potentially one of the largest sources of phase error. In all baseline tests, an image of an HQSG was projected onto a planar surface and imaged with an 8-bit camera-digitization board combination. The image-plane spacing of the fringe pattern is approximately 10 pixels, and the minimum contrast is approximately 120 gray levels, giving a minimum signal amplitude of 60 gray levels, which corresponds to approximately 7-bit digitization with maximum contrast. Because the measured noise in real images is due to a combination of both temporal and spatial variations in intensity, the relative magnitude of each term is of interest in this study.

TEMPORAL NOISE

As noted previously, the standard deviation in intensity due to temporal random noise was approximately 0.9 gray levels before averaging. Thus, the ratio between standard deviation and minimum amplitude is ~ 1.7 percent. For dynamic applications, this level of noise is expected to be present in single-image measurements.

To demonstrate the effectiveness of time averaging in temporal noise reduction, image averaging was performed on the projected fringe images using a series of 500 images acquired at 25 Hz. Results from these experiments demonstrated that the standard deviation in the resulting intensity pattern is proportional to approximately $N^{-0.50}$ for $N < 200$, which is consistent with statistical theory for variability of the mean value. Therefore, a portion of the variability in the intensity data is due to temporal random noise in the intensity pattern; when possible, image averaging can be used to reduce the errors associated with this form of temporal noise.

SPATIALLY-VARYING NOISE

To estimate the effect of spatially varying noise on the error of phase extraction in a real image with unknown phase distribution, the following process is used. First, a total of 100 images are averaged to minimize temporal noise in the intensity data. Second, assuming that the phase distribution is a continuous function, the phase of one row in the image is extracted using (1) the Hilbert filter with a Laplacian pyramid, (2) unwrapped and (3) fitted with a fourth-order polynomial. Third, the difference between this polynomial and the scattered, unwrapped phase data is considered as the
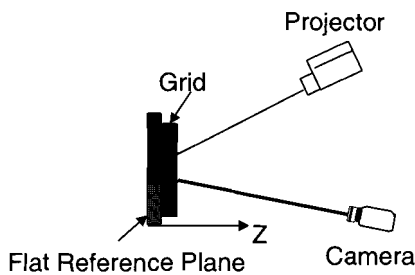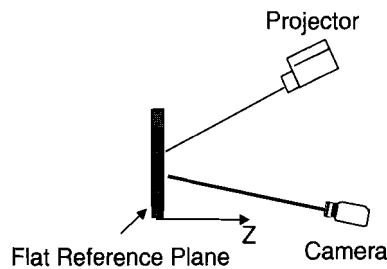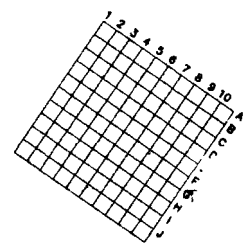
Fig. 9—(a) Schematic of the setup for calibration of camera parameters, (b) schematic for calibration of the height-phase relationship, (c) binarized image of precision grid used in calibration
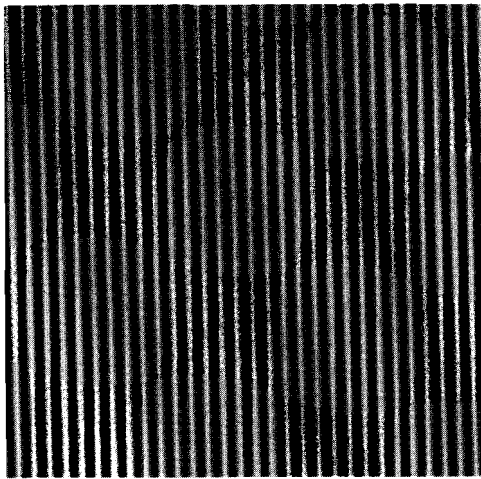

Fig. 10—An 8-bit image of a fringe pattern taken by a CCD camera

error of phase extraction. This approach has been verified by extraction and analysis of phase information from a generated image.

The procedure outlined above was used to extract the phase from a time-averaged real image that is similar to the one shown in Fig. 10. Results from the analysis indicate that the maximum and the standard deviation in phase error are approximately 0.075 radians and 0.03 radians, respectively. Comparison of these values to simulation data in Fig. 8 shows that the measurement error values are reasonably close to the simulation predictions of 0.05 for the maximum error and 0.02 for the standard deviation.

It is worth noting that the use of fringe images that were not time averaged resulted in maximum phase error and standard deviation in phase of approximately 0.08 and 0.035, respectively. These results indicate that a major source of error in the extraction of phase is random spatial fluctuations in intensity values.

CONTRAST VARIATIONS

Because contrast variations may affect the accuracy of the height measurements, primarily through reduced accuracy in the phase extraction process, experiments were performed in which fringe pattern contrast was altered. Because experimental phase measurements will include errors from both spatially varying noise (e.g., due to reflectivity changes on the object surface) and contrast changes, numerical estimates for the combined effects of both variables will be compared to the experimental data.

Using an experimental arrangement similar to the one shown in Fig. 1, a planar object was illuminated with a projected fringe pattern using the HQSG. Time-averaged images were acquired with three different lens apertures to provide a range of fringe pattern contrast. Typical experimental parameters for this work include a fringe spacing of 16 pixels/fringe on the sensor array, a distance from the lens to the object of ≈ 600 mm, a camera oriented nearly perpendicular to the object plane and a projector rotated ≈ 25 deg from the normal to the object plane. Each image was obtained by averaging 100 consecutive images. Phase extraction followed the procedures outlined previously and included use of both a Hilbert filter with Laplacian pyramid algorithm and a flood-fill approach for phase unwrapping.

For comparison to the measured phase data, numerical simulations were performed using both the measured intensity contrast and the measured intensity variations. The numerical simulations assumed uniform contrast, with additive random intensity noise having the same standard deviation as the measured data.

The data for intensity contrast and intensity noise from all three experiments are shown in Table 1. In addition, a comparison of the predicted and measured maximum phase error and standard deviation in phase for three separate experiments are shown in Table 1.

As shown in Table 1, the simulation results and experimental measurements are in good agreement for all three experiments. Furthermore, the results demonstrate that a combination of significant contrast reduction and spatially varying noise will dramatically increase the phase extraction error. Specifically, to ensure that the standard deviation in phase error is below 0.042 radians, image contrast must be ≈ 70 gray levels and the noise-to-signal ratio must be less than ≈ 2.25 percent.

FRINGE SPACING

Using an experimental arrangement similar to the one shown in Fig. 1, a diffuse planar object was illuminated with a projected fringe pattern using the HQSG. To obtain a wide range of intensity pattern frequencies in the image plane, the zoom of the camera lens and object distance were varied. Typical experimental parameters for these experiments were (1) object distances from 400 to 600 mm, (2) camera oriented nearly perpendicular to the object plane and (3) projector rotated ≈ 25 deg from the normal to the object plane.

		Fringe Pattern 1	Fringe Pattern 2	Fringe Pattern 3
Maximum error in phase (radians)	Simulation	0.070	0.090	0.187
	Experiment	0.100	0.127	0.193
Standard deviation of error in phase (radians)	Simulation	0.035	0.047	0.052
	Experiment	0.040	0.048	0.056
Mean value of amplitude (gray level)		70.37	49.73	12.56
Standard deviation of amplitude (gray level)		1.57	1.41	0.70
Ratio between standard deviation of noise to the amplitude of the signal (percentage)		2.23	2.84	5.57

To minimize the effects of temporal noise, each image was obtained by averaging 100 consecutive images. In all cases, the contrast is on the order of 70 gray levels and the noise-to-signal ratio is $\approx$ 2.2 percent to minimize errors due to contrast and spatial noise. Phase extraction followed the procedures presented earlier in the section on the Hilbert transform.

Table 2 presents a comparison of the experimental results of the analytical predictions for image plane fringe spacing of 9, 21, 30 and 35 pixels, respectively. As shown in Table 2, the increase in experimental error that occurs as the fringe spacing increases is in very good agreement with simulation predictions. Furthermore, the results demonstrate that a combination of large fringe spacing and spatially varying noise can introduce large errors in phase. To ensure that the standard deviation in phase error is below 0.042 radians, fringe spacing must be in the range 3 to 31 pixels while controlling both contrast and intensity noise.

Experimental Validation Experiments

In this section, two tests were performed with the fringe projection system shown in Fig. 1 to obtain spatial (X, Y, Z) data. For comparison, a coordinate measurement machine (CMM) was used to independently measure height data. The tests included measurement of a planar object in two positions and measurement of a portion of a turbine blade. Direct comparisons of the independent measurements are provided to demonstrate the accuracy of the fringe projection method and simulations.

Planar Object

A 100 $\times$ 100 mm diffusely reflecting planar object was used in these tests. Images were acquired of a 50 $\times$ 50 mm subregion in two positions. One position was normal to the camera, and the second position was tilted toward the camera $\sim$ 3 deg. Setup parameters for the test included an object surface fringe spacing of approximately 0.6 mm (fringe density of 9 pixels/fringe), fringe contrast of approximately 125 gray levels, time-varying noise of approximately 1 gray level (standard deviation) and spatially varying noise of approximately 2.3 gray levels (standard deviation). A Pulnix digital camera with 768 $\times$ 484 spatial resolution and 8-bit intensity resolution was used to record digital images of the fringe patterns.

Camera calibration followed the procedure outlined previously, and the resulting camera parameters are shown in Table 3. Figure 11 shows a typical phase-height relationship calibration curve obtained when using a reference plane translated perpendicular to the surface within the calibration range.

The four coefficients for the fitted third-order polynomial in Fig. 11 are $A_0 = -1.458E - 03$, $A_1 = 1.167E - 01$, $A_2 = -1.793E - 05$ and $A_3 = -1.554E - 09$. It is noted that the second- and third-order coefficients are very small relative to the first-order coefficient and that the phase-height relationship curve is almost linear. Practically, third-order polynomial fitting is sufficient for most purposes because the difference between second- and third-order polynomial fits is on the order of 3 μm. However, it is easily verified that use of a linear fit instead of second- or third-order polynomials may cause errors up to 200 μm.

Using these results, profiles of the plane before and after tilting are obtained and the (X, Y, Z) coordinates are fitted with a least squares plane. The residuals of the fitted data relative to the measurements for both planes are given in Table 3.

Independent measurement of the planar surface profile by CMM was performed for comparison to the fringe projection data. Using a least squares planar fit to approximately 100 CMM data points, the surface fit indicated that the standard deviation was $\approx$ 8μm, which is in reasonable
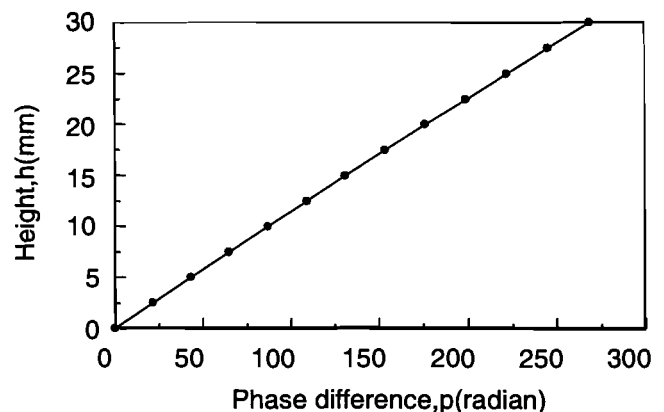

Fig. 11—A typical phase-height relationship

TABLE 2—MEASUREMENTS AND PREDICTIONS FOR FRINGE PATTERNS WITH VARIOUS COMBINATIONS OF FRINGE SPACING AND INTENSITY NOISE

		Fringe Pattern 1	Fringe Pattern 2	Fringe Pattern 3	Fringe Pattern 4
Maximum error in phase (radians)	Simulation	0.07	0.068	0.067	0.3
	Experiment	0.10	0.075	0.081	0.17
Standard deviation of error in phase (radians)	Simulation	0.035	0.038	0.037	0.052
	Experiment	0.040	0.042	0.0408	0.062
Fringe spacing (pixels)		9	21	30	35
Mean value of amplitude (gray level)		70.37	69.02	70.15	72.01
Standard deviation amplitude (gray level)		1.57	1.50	1.53	1.58
Ratio of standard deviation and noise and signal (percentage)		2.23	2.17	2.18	2.19

TABLE 3—RESULTS OF BASELINE PROFILE MEASUREMENT WITH THE FRINGE PROJECTION METHOD

		Plane	Tilted Plane
Angle ξ(deg)		48.203	
Angle η(deg)		4.001	
Angle χ(deg)		−0.529	
Pinhole distance of camera (pixels)		2.759×10^4	
Distance Z (from camera to calibration plane, mm)		679.7	
Angle α(deg)		~25.0	
Fitting coefficients	A	2.199	3.483
	B	1.26×10^{-3}	-1.54×10^{-2}
	C	4.5×10^{-4}	-3.58×10^{-4}
Residual relative to fitting function	Maximum (μm)	30.6	26.3
	Minimum (μm)	−36.8	−37.9
	Mean (μm)	0	0
	Standard deviation (μm)	6.5	6.3

agreement with fringe projection measurements. Because manufacturer's specifications for the CMM included an error estimate of $\pm 8.7 \mu$m for each CMM measurement point, the flatness of the plate could not be determined with higher accuracy. Finally, inspection of the error distribution for the fringe projection data indicates that it is randomly distributed throughout the measurement region.

Turbine Blade

Figure 12 shows the region of a turbine blade that was chosen for profiling, along with a close-up of the region of interest after illumination by the projected fringe pattern. Analysis of the surface shape data indicates that the maximum height change is ∼ 4.7 mm and the minimum radius of curvature is ∼ 12.1 mm.

Table 4 presents the parameters used in the experimental setup to measure the three-dimensional shape of the turbine blade. For the setup parameters shown in Table 4, the estimated standard deviation of the measurements is ≈ 10μm.

For direct comparison to the measured turbine blade data, independent measurements of the same region on the turbine blade were obtained using a CMM. Two hundred CMM measurements were obtained for the turbine blade. Due to curvature variations on the object surface and the presence of a 7.5 mm spherical ball at the end of the surface probe, the CMM measurements for the coordinate of the center of

the ball were modified to improve the accuracy of the surface positions for the curved turbine blade. The procedure used to improve the CMM measurement accuracy is as follows.

Assuming that the surface height data are $z = z(x, y)$ and the center of the ball is (x_c, y_c, z_c), then along a line on the surface, one can write

$$
\begin{cases}
\dfrac{x_c - x}{\dfrac{\partial z}{\partial x}} = \dfrac{y_c - y}{\dfrac{\partial z}{\partial y}} \\
\dfrac{y_c - y}{\dfrac{\partial z}{\partial y}} = \dfrac{z_c - z}{-1}
\end{cases}
\tag{16}
$$

Also, the spherical surface can be written in the following form:

$$(x_c - x)^2 + (y_c - y)^2 + (z_c - z)^2 = R^2. \tag{17}$$

Approximating the derivatives for the true surface with derivatives on the surface obtained using the CMM measurements, one can write

$$\frac{\partial z}{\partial x} \approx \frac{\partial z_c}{\partial x_c} = p \quad \frac{\partial z}{\partial y} \approx \frac{\partial z_c}{\partial y_c} = q. \tag{18}$$

Provided that both R and the CMM data set $[(x_c)_i, (y_c)_i, (z_c)_i]$, $i = 1, 2, \ldots, m$, are known, the true coordinates of the surface can be estimated using eqs (16)-(18) to give

TABLE 4—SETUP PARAMETERS AND ERROR ESTIMATES FOR BLADE PROFILE MEASUREMENTS

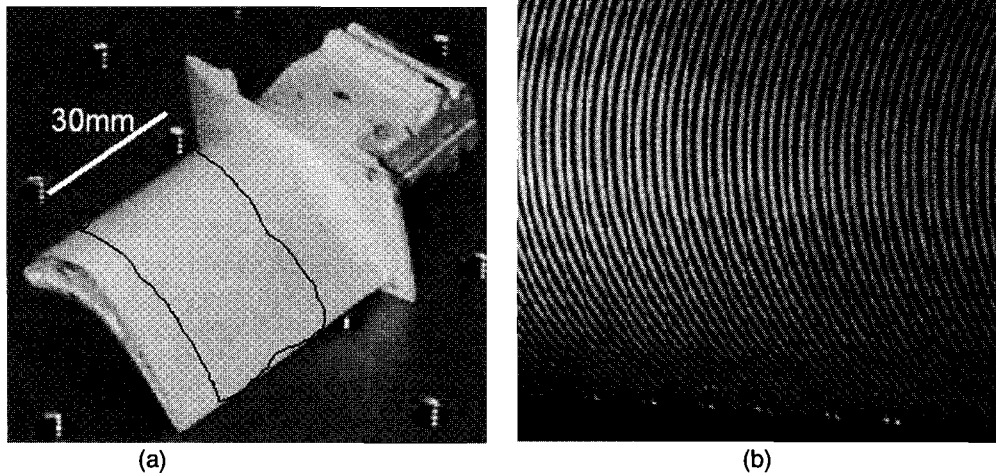|		
Angle ξ(deg)		−34.55
Angle η(deg)		−7.383
Angle χ(deg)		0.975
Pinhole distance of camera (pixels)		2.803×10^4
Distance Z (from camera to calibration plane, mm)		1301
Angle α(deg)		≈25
Object surface fringe spacing (f/mm)		≈0.652
Error in phase (radians)	Maximum	0.087
	Minimum	−0.08
	Standard deviation	0.04

Fig. 12—Painted turbine blade with selected measurement region (a) and projected fringe pattern (b)

$$\begin{cases} x = x_c + \dfrac{pR}{\sqrt{1 + p^2 + q^2}} \\ y = y_c + \dfrac{qR}{\sqrt{1 + p^2 + q^2}} \\ z = z_c - \dfrac{R}{\sqrt{1 + p^2 + q^2}} \end{cases} \quad , \qquad (19)$$

where eq (19) is accurate everywhere away from sharp edges, with the error in (x, y, z) being on the same order as the accuracy in determining (x_c, y_c, z_c).

Using eqs (16) to (19), the CMM measurements over a 24.6×24.3 mm patch on the turbine blade were converted into a final data set. Figure 13 shows the full-field comparison of the two data sets after optimal registration of the two data sets and the relative error between the two data sets along one line. In Fig. 13, the regions of mismatch appear in lighter tone.

Results indicate that the average error between all matching points on the two surfaces is 19.7 μm after optimal registration was completed. Because the estimated error in the fringe pattern measurement is ±10μm and the specified CMM accuracy is ±8.7μm, the difference between the two data sets after registration is consistent with a Euclidean norm error estimate for the combined data sets of 13.3 μm.

Summary

An accurate camera calibration procedure and improved phase extraction procedures using a modified Hilbert transform with Laplacian pyramid algorithms were developed and successfully demonstrated for measurement of the full (X, Y, Z) positions of surface points using single-frequency fringe projection profiling methods. Detailed numerical simulations and controlled baseline experiments were performed to quantify the key error sources in the measurement process and verify the accuracy of the approach.

Simulation results indicate that for fringe patterns having sensor plane fringe spacing from 3 to 30 pixels, the resulting phase error can be reduced to less than 0.02 radians provided that the spatial frequency of the background intensity variations meets the inequality $k = 2\pi/\lambda < 0.01$ pixels^{-1}, the recorded fringe patterns have an amplitude of at least 64 gray levels and the recorded fringe patterns have a random noise of less than 1 percent of the signal amplitude. These results can be converted into requirements on experimental parameters (e.g., image magnification, object surface preparation, projection angle, surface curvature) to ensure optimum accuracy.

Baseline experiments were performed that demonstrate that the error sources (e.g., random intensity fluctuations, contrast reduction) quantified in the numerical simulations are in good agreement with physical measurements. Specifically, results indicate random spatial changes in the intensity pattern due to variations in object surface reflectivity introduce negligible bias and a random variation of 0.05 radians in the extracted phase for almost all experiments performed.

To demonstrate the method for applications, spatial (X, Y, Z) data were obtained by both CMM and fringe projection for both a planar surface and a turbine blade.
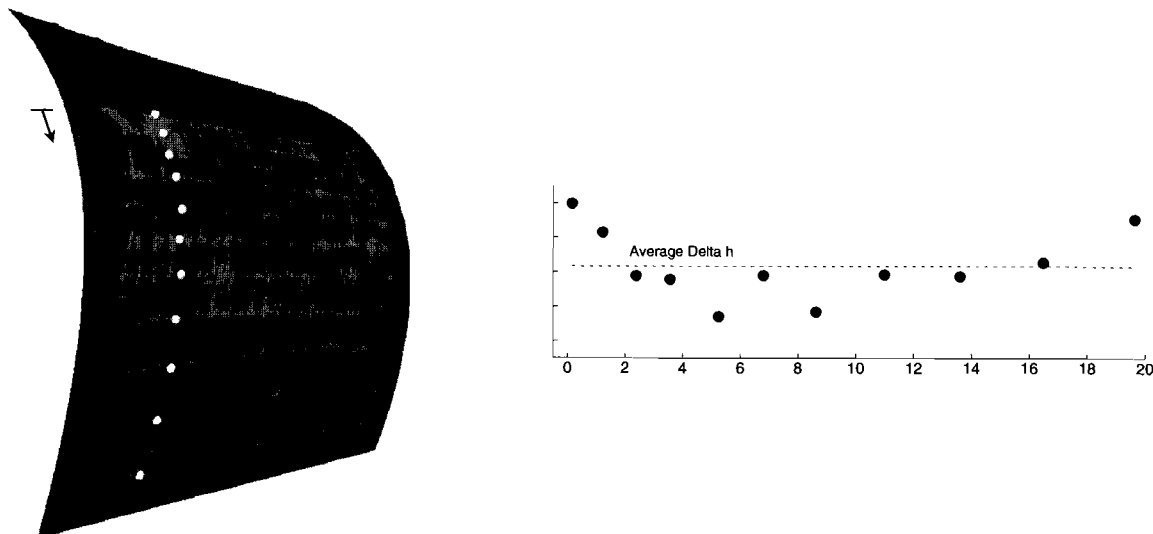
Fig. 13—(a) Measured shape after registration of coordinate measurement machine and fringe projection data, (b) difference in measured height along one line

Results indicate that the CMM measurements are in good agreement with fringe projection data for both cases and that simulation estimates for the fringe projection errors are consistent with measurements.

Taken together, the experimental studies and numerical simulations confirm that very high accuracy shape measurements can be made with single-frequency projected grids. Specifically, phase errors of less than 0.04 radians on a pixel-by-pixel basis are achievable for a wide range of fringe density using the proposed method. Furthermore, the experimental and numerical results demonstrate conclusively that it is possible to design both a fringe projection system and a measurement process to achieve a prespecified accuracy and resolution in the point-to-point measurement of the spatial (X, Y, Z) positions.

Acknowledgments

References

1. McNeill, S.R., Sutton, M.A., Miao, Z., and Ma, J., "Measurement of Surface Profile Using Digital Image Correlation," EXPERIMENTAL MECHANICS, 37 (1), 13–21 (1997).

2. Helm, J.D., Sutton, M.A., and McNeill, S.R., "Improved Three-dimensional Image Correlation for Surface Displacement Measurement," Opt. Eng., 35, 1911–1920 (1996).

3. Tsai, R.Y., "An Efficient and Accurate Camera Calibration Technique for 3D Machine Vision," Proceedings of the IEEE International Conference on Computer Vision and Pattern Recognition, 364–374 (1986).

4. Weng, J., Cohen, P., and Herniou, M., "Camera Calibration with Distortion Models and Accuracy Evaluation," IEEE Trans. Pattern Anal. Mach. Intell., 14, 965–980 (1992).

5. Takasaki, M., "Moiré Topography," Appl. Opt., 9, 1467–1472 (1970).

6. Masanoril, I., Toyohiko, Y., and Takashi, S., "Scanning Moiré Method and Automatic Measurement of 3-D Shapes," Appl. Opt., 6, 2152–2162 (1976).

7. Matssumoto, T., Kitagawa, Y., Adachi, M., and Hayashi, A., "Moiré Topography for Three-dimensional Profile Measurement Using the Interference Fringes," Opt. Eng., 31, 2668–2672 (1992).

8. Suganuma, M. and Yoshizawa, T., "Three-dimensional Shape Analysis by Use of a Projected Grating Image," Opt. Eng., 30, 1529–1533 (1991).

9. Larkin, K.G. and Oreb, B.F., "Design and Assessment of Symmetrical Phase-shifting Algorithms," J. Opt. Soc. Am., 9, 1741–1748 (1992).

10. Hibino, K., Oreb, B.F., and Farrant, D.I., "Phase Shifting for Non-sinusoidal Waveforms with Phase-shifting Errors," J. Opt. Soc. Am., 12, 761–768 (1995).

11. Zhao, B. and Surrel, Y., "Effects of Quantization Error on the Computed Phase of Phase-shifting Measurements," Appl. Opt., 36, 2070–2075 (1997).

12. Hibino, K., Oreb, B.F., Farrant, D., and Larkin, K.G., "Phase-shifting Algorithms for Nonlinear and Spatially Nonuniform Phase Shifts," J. Opt. Soc. Am., 14, 918–930 (1997).

13. Hibino, K., Larkin, K.G., Oreb, B.F., and Farrant, D.I., "Phase-shifting Algorithms for Nonlinear and Spatially Nonuniform Phase Shifts: Reply to Comment," J. Opt. Soc. Am., 15, 1234–1235 (1998).

14. Huang, P.S., Jin, F., and Chiang, F.P., "Quantitative NDE of Corrosion by Digital Fringe Projection and Phase Shifting," Proceedings of the SEM Spring Conference on Experimental and Applied Mechanics, Houston, TX, 305–306 (June 1998).

15. Huntley, J.M. and Coggrave, C.R., "High Speed Measurement of Discontinuous Surface Profiles," International Union of Theoretical and Applied Mechanics Symposium on Advanced Optical Methods and Applications in Solid Mechanics, Poitiers-Futuroscope, France, 161–168 (Aug.-Sep. 1998).

16. Hornbeck, L.J., "Digital Light Processing for High-brightness, High-resolution Applications," Proc. SPIE, 3013, 27–40 (1997).

17. Kato, J., Yamaguchi, I., Nakamura, T., and Kuwashima, S., "Video-rate Fringe Analyzer Based on Phase-shifting Electronic Moiré Patterns," Appl. Opt., 36, 8403–8412 (1997).

18. Takeda, M., Ika, H., and Kobayasha, S., "Fourier Transform Method of Fringe Pattern Analysis for Computer Based Topography and Interferometry," J. Opt. Soc. Am., 72, 156–160 (1982).

19. Zweig, D.A. and Hufnagel, R.E., "A Hilbert Transform Algorithm for Fringe-pattern Analysis," Adv. Opt. Manufact. Test., **SPIE 1333**, 295–302 (1990).

20. Jaehne, B., Practical Handbook on Image Processing for Scientific Applications, Chemical Rubber Company Press, Cleveland, OH (1997).

21. Tang, S. and Hung, Y.Y., "Fast Profilometer for the Automatic Measurement of 3-D Object Shapes," Appl. Opt., **29**, 3012–3018 (1990).

22. Toyooka, S. and Iwasa, Y., "Automatic Profilometry of 3-D Diffuse Objects by Spatial Phase Detection," Appl. Opt., **25**, 1630–1633 (1986).

23. Gu, R., Yoshizawa, T., and Otani, Y., "One-step Phase Shift 3-D Surface Profilometry with Grating Projection," Appl. Opt., **21** (1-2), 61–75 (1994).

24. Burt, P.J. and Adelson, E.H., "The Laplacian Pyramid as a Compact Image Code," IEEE Trans. Commun., **31**, 532–540 (1983).

25. Huntley, J.M., "Noise-immune Phase Unwrapping Algorithm," Appl. Opt., **28**, 3268–3270 (1989).

26. Bone, D.J., "Fourier Fringe Analysis—The 2-dimensional Phase Unwrapping Problem," Appl. Opt., **30**, 3627–3632 (1991).

27. Carter, W.H., "On Unwrapping 2-dimensional Phase Data in Contour Maps," Opt. Commun., **94** (1-3), 1–7 (1992).

28. Judge, T.R. and Bryanstoncross, P.J., "A Review of Phase Unwrapping Techniques in Fringe Analysis," Opt. Lasers Eng., **21**, 199–239 (1994).

29. Cusack, R., Huntley, J.M., and Goldrein, H.T., "Improved Noise-immune Phase-unwrapping Algorithm," Appl. Opt., **34**, 781–789 (1995).

30. Huntley, J.M. and Saldner, H.O., "Shape Measurement Temporal Phase Unwrapping: Comparison of Unwrapping Algorithms," Meas. Sci. Tech., **8**, 986–992 (1997).

31. Fujigaki, M. and Morimoto, Y., "Automated Shape Analysis for Multiple Phase Fringes by Phase-shifting Method Using Fourier Transform," Proceedings of the 11th International Conference on Experimental Mechanics, **1**, Oxford, UK, 711–715 (Aug. 1998).